

(CdSe)ZnS Core–Shell Quantum Dots: Synthesis and Characterization of a Size Series of Highly Luminescent Nanocrystallites

B. O. Dabbousi,[†] J. Rodriguez-Viejo,[‡] F. V. Mikulec,[†] J. R. Heine,[§] H. Mattoussi,[§] R. Ober,[⊥] K. F. Jensen,^{‡,§} and M. G. Bawendi^{*,†}

Departments of Chemistry, Chemical Engineering, and Materials Science and Engineering, Massachusetts Institute of Technology, 77 Massachusetts Ave., Cambridge, Massachusetts 02139, and Laboratoire de Physique de la Matière Condensée, Collège de France, 11 Place Marcellin Berthelot, 75231 Paris Cedex 05, France

Received: March 27, 1997; In Final Form: June 26, 1997[⊗]

We report a synthesis of highly luminescent (CdSe)ZnS composite quantum dots with CdSe cores ranging in diameter from 23 to 55 Å. The narrow photoluminescence (fwhm \leq 40 nm) from these composite dots spans most of the visible spectrum from blue through red with quantum yields of 30–50% at room temperature. We characterize these materials using a range of optical and structural techniques. Optical absorption and photoluminescence spectroscopies probe the effect of ZnS passivation on the electronic structure of the dots. We use a combination of wavelength dispersive X-ray spectroscopy, X-ray photoelectron spectroscopy, small and wide angle X-ray scattering, and transmission electron microscopy to analyze the composite dots and determine their chemical composition, average size, size distribution, shape, and internal structure. Using a simple effective mass theory, we model the energy shift for the first excited state for (CdSe)ZnS and (CdSe)-CdS dots with varying shell thickness. Finally, we characterize the growth of ZnS on CdSe cores as locally epitaxial and determine how the structure of the ZnS shell influences the photoluminescence properties.

I. Introduction

Semiconductor nanocrystallites (quantum dots) whose radii are smaller than the bulk exciton Bohr radius constitute a class of materials intermediate between molecular and bulk forms of matter.¹ Quantum confinement of both the electron and hole in all three dimensions leads to an increase in the effective band gap of the material with decreasing crystallite size. Consequently, both the optical absorption and emission of quantum dots shift to the blue (higher energies) as the size of the dots gets smaller. Although nanocrystallites have not yet completed their evolution into bulk solids, structural studies indicate that they retain the bulk crystal structure and lattice parameter.² Recent advances in the synthesis of highly monodisperse nanocrystallites^{3–5} have paved the way for numerous spectroscopic studies^{6–11} assigning the quantum dot electronic states and mapping out their evolution as a function of size.

Core–shell type composite quantum dots exhibit novel properties making them attractive from both an experimental and a practical point of view.^{12–19} Overcoating nanocrystallites with higher band gap inorganic materials has been shown to improve the photoluminescence quantum yields by passivating surface nonradiative recombination sites. Particles passivated with inorganic shell structures are more robust than organically passivated dots and have greater tolerance to processing conditions necessary for incorporation into solid state structures. Some examples of core–shell quantum dot structures reported earlier include CdS on CdSe and CdSe on CdS,¹² ZnS grown on CdS,¹³ ZnS on CdSe and the inverse structure,¹⁴ CdS/HgS/CdS quantum dot quantum wells,¹⁵ ZnSe overcoated CdSe,¹⁶ and SiO₂ on Si.^{17,18} Recently, Hines and Guyot-Sionnest

reported making (CdSe)ZnS nanocrystallites whose room temperature fluorescence quantum yield was 50%.¹⁹

This paper describes the synthesis and characterization of a series of room-temperature high quantum yield (30%–50%) core–shell (CdSe)ZnS nanocrystallites with narrow band edge luminescence spanning most of the visible spectrum from 470 to 625 nm. These particles are produced using a two-step synthesis that is a modification of the methods of Danek et al.¹⁶ and Hines et al.¹⁹ ZnS overcoated dots are characterized spectroscopically and structurally using a variety of techniques. The optical absorption and photoluminescence spectra of the composite dots are measured, and the lowest energy optical transition is modeled using a simplified theoretical approach. Wavelength dispersive X-ray spectroscopy and X-ray photoelectron spectroscopy are used to determine the elemental and spatial composition of ZnS overcoated dots. Small-angle X-ray scattering in solution and in polymer films and high-resolution transmission electron microscopy measurements help to determine the size, shape, and size distribution of the composite dots. Finally, the internal structure of the composite quantum dots and the lattice parameters of the core and shell are determined using wide-angle X-ray scattering.

In addition to having higher efficiencies, ZnS overcoated particles are more robust than organically passivated dots and potentially more useful for optoelectronic device structures. Electroluminescent devices (LED's) incorporating (CdSe)ZnS dots into heterostructure organic/semiconductor nanocrystallite light-emitting devices may show greater stability.²⁰ Thin films incorporating (CdSe)ZnS dots into a matrix of ZnS using electrospray organometallic chemical vapor deposition (ES-OMCVD) demonstrate more than 2 orders of magnitude improvement in the PL quantum yields (\sim 10%) relative to identical structures based on bare CdSe dots.²¹ In addition, these structures exhibit cathodoluminescence²¹ upon excitation with high-energy electrons and may potentially be useful in the

* To whom correspondence should be addressed.

[†] Department of Chemistry, MIT.

[‡] Department of Chemical Engineering, MIT.

[§] Department of Materials Science and Engineering, MIT.

[⊥] Collège de France.

[⊗] Abstract published in *Advance ACS Abstracts*, September 1, 1997.

production of alternating current thin film electroluminescent devices (ACTFELD).

II. Experimental Section

Materials. Trioctylphosphine oxide (TOPO, 90% pure) and trioctylphosphine (TOP, 95% pure) were obtained from Strem and Fluka, respectively. Dimethylcadmium (CdMe_2) and diethylzinc (ZnEt_2) were purchased from Alfa and Fluka, respectively, and both materials were filtered separately through a 0.2 μm filter in an inert atmosphere box. Trioctylphosphine selenide was prepared by dissolving 0.1 mol of Se shot in 100 mL of TOP, thus producing a 1 M solution of TOPSe. Hexamethyldisilathiane ($(\text{TMS})_2\text{S}$) was used as purchased from Aldrich. HPLC grade *n*-hexane, methanol, pyridine, and 1-butanol were purchased from EM Sciences.

Synthesis of Composite Quantum Dots. $(\text{CdSe})/\text{ZnS}$. Nearly monodisperse CdSe quantum dots ranging from 23 to 55 Å in diameter were synthesized via the pyrolysis of the organometallic precursors, dimethylcadmium and trioctylphosphine selenide, in a coordinating solvent, trioctylphosphine oxide (TOPO), as described previously.³ The precursors were injected at temperatures ranging from 340 to 360 °C, and the initially formed small ($d = 23$ Å) dots were grown at temperatures between 290 and 300 °C. The dots were collected as powders using size-selective precipitation³ with methanol and then redispersed in hexane.

A flask containing 5 g of TOPO was heated to 190 °C under vacuum for several hours and then cooled to 60 °C after which 0.5 mL of trioctylphosphine (TOP) was added. Roughly 0.1–0.4 μmol of CdSe dots dispersed in hexane was transferred into the reaction vessel via syringe, and the solvent was pumped off.

Diethylzinc (ZnEt_2) and hexamethyldisilathiane ($(\text{TMS})_2\text{S}$) were used as the Zn and S precursors. The amounts of Zn and S precursors needed to grow a ZnS shell of desired thickness for each CdSe sample were determined as follows: First, the average radius of the CdSe dots was estimated from TEM or SAXS measurements. Next, the ratio of ZnS to CdSe necessary to form a shell of desired thickness was calculated based on the ratio of the shell volume to that of the core assuming a spherical core and shell and taking into account the bulk lattice parameters of CdSe and ZnS. For larger particles the ratio of Zn to Cd necessary to achieve the same thickness shell is less than for the smaller dots. The actual amount of ZnS that grows onto the CdSe cores was generally less than the amount added due to incomplete reaction of the precursors and to loss of some material on the walls of the flask during the addition.

Equimolar amounts of the precursors were dissolved in 2–4 mL of TOP inside an inert atmosphere glovebox. The precursor solution was loaded into a syringe and transferred to an addition funnel attached to the reaction flask. The reaction flask containing CdSe dots dispersed in TOPO and TOP was heated under an atmosphere of N_2 . The temperature at which the precursors were added ranged from 140 °C for 23 Å diameter dots to 220 °C for 55 Å diameter dots.²² When the desired temperature was reached, the Zn and S precursors were added dropwise to the vigorously stirring reaction mixture over a period of 5–10 min.

After the addition was complete, the mixture was cooled to 90 °C and left stirring for several hours. A 5 mL aliquot of butanol was added to the mixture to prevent the TOPO from solidifying upon cooling to room temperature. The overcoated particles were stored in their growth solution to ensure that the surface of the dots remained passivated with TOPO. They were later recovered in powder form by precipitating with methanol and redispersed into a variety of solvents including hexane, chloroform, toluene, THF, and pyridine.

$(\text{CdSe})/\text{CdS}$. Cadmium selenide nanocrystallites with diameters between 33.5 and 35 Å were overcoated with CdS to varying thickness using the same basic procedure as that outlined for the ZnS overcoating. The CdS precursors used were $\text{Me}_2\text{-Cd}$ and $(\text{TMS})_2\text{S}$. The precursor solution was dripped into the reaction vessel containing the dots at a temperature of 180 °C and a rate of ~ 1 mL/min. The solution became noticeably darker as the overcoat precursors were added. Absorption spectra taken just after addition of precursors showed a significant shift in the absorption peak to the red. To store these samples, it was necessary to add equal amounts of hexane and butanol since the butanol by itself appeared to flocculate the particles.

Optical Characterization. UV–vis absorption spectra were acquired on an HP 8452 diode array spectrophotometer. Dilute solutions of dots in hexane were placed in 1 cm quartz cuvettes, and their absorption and corresponding fluorescence were measured. The photoluminescence spectra were taken on a SPEX Fluorolog-2 spectrometer in front face collection mode. The room-temperature quantum yields were determined by comparing the integrated emission of the dots in solution to the emission of a solution of rhodamine 590 or rhodamine 640 of identical optical density at the excitation wavelength.

Wavelength Dispersive X-ray Spectroscopy. A JEOL SEM 733 electron microprobe operated at 15 kV was used to determine the chemical composition of the composite quantum dots using wavelength dispersive X-ray (WDS) spectroscopy. One micrometer thick films of $(\text{CdSe})/\text{ZnS}$ quantum dots were cast from concentrated pyridine solutions onto Si(100) wafers, and after the solvent had completely evaporated the films were coated with a thin layer of amorphous carbon to prevent charging.

X-ray Photoelectron Spectroscopy. XPS was performed using a Physical Electronics 5200C spectrometer equipped with a dual X-ray anode (Mg and Al) and a concentric hemispherical analyzer (CHA). Data were obtained with Mg $K\alpha$ radiation (1253.6 eV) at 300 W (15 keV, 20 mA). Survey scans were collected over the range 0–1100 eV with a 179 eV pass energy detection, corresponding to a resolution of 2 eV. Close-up scans were collected on the peaks of interest for the different elements with a 71.5 eV pass energy detection and a resolution of 1 eV. A base pressure of 10^{-8} Torr was maintained during the experiments. All samples were exchanged with pyridine and spin-cast onto Si substrates, forming a thin film several monolayers thick.

Transmission Electron Microscopy. A Topcon EM002B transmission electron microscope (TEM) was operated at 200 kV to obtain high-resolution images of individual quantum dots. An objective aperture was used to selectively image the (100), (002), and (101) wurtzite lattice planes. The samples were prepared by placing one drop of a dilute solution of dots in octane onto a copper grid supporting a thin film of amorphous carbon and then wicking off the remaining solvent after 30 s. A second thin layer of amorphous carbon was evaporated onto the samples in order to minimize charging and reduce damage to the particles caused by the electron beam.

Small-Angle X-ray Scattering (SAXS) in Polymer Films. Small-angle X-ray scattering (SAXS) samples were prepared using either poly(vinyl butyral) (PVB) or a phosphine-functionalized diblock copolymer [methyltetraacyclododecene]₃₀₀–[norbornene– $\text{CH}_2\text{O}(\text{CH}_2)_5\text{P}(\text{oct})_2$]₂₀, abbreviated as $(\text{MTD}_{300}\text{P}_{20})$, as the matrix.²³ Approximately 5 mg of nanocrystallites of dispersed in 1 mL of toluene, added to 0.5 mL of a solution containing 10 wt % PVB in toluene, concentrated under vacuum to give a viscous solution, and then cast onto a silicon wafer. The procedure is the same for $\text{MTD}_{300}\text{P}_{20}$, except THF is used

as the solvent for both nanocrystallites and polymer. The resulting $\sim 200\ \mu\text{m}$ thick film is clear to slightly opaque. X-ray diffraction spectra were collected on a Rigaku 300 Rotaflex diffractometer operating in the Bragg configuration using Cu K α radiation. The accelerating voltage was set at 60 kV with a 300 mA flux. Scatter and diffraction slits of $1/6^\circ$ and a 0.3 mm collection slit were used.

Small-Angle X-ray Scattering in Dilute Solutions. The X-ray source was a rotating copper anode operated at 40 kV and 25 mA. The apparent point source (electron beam irradiated area on the anode) was about $10^{-2}\ \text{mm}^2$. The beam was collimated onto a position sensitive detector, PSPE (ELPHYSE). A thin slit, placed before the filter, selects a beam with the dimensions of $3 \times 0.3\ \text{mm}^2$ on the detector. The position sensitive linear detector has a useful length of 50 mm, placed at a distance $D = 370\ \text{mm}$ from the detector. The spatial resolution on the detector is $200\ \mu\text{m}$. This setup allows a continuous scan of scattering wavevectors between 6×10^{-3} and $0.40\ \text{\AA}^{-1}$, with a resolution of about $3 \times 10^{-3}\ \text{\AA}^{-1}$.

The samples used were quartz capillary tubes with about 1 mm optical path, filled with the desired dispersion, and then flame-sealed after filling. The intensity from the reference, I_{ref} , is collected first, and then the intensity from the sample, I_s . The intensity used in the data analysis is the difference: $I = I_s - I_{\text{ref}}$.

Wide-Angle X-ray Scattering (WAXS). The wide-angle X-ray powder diffraction patterns were measured on the same setup as the SAXS in polymer dispersions. The TOPO/TOP capped nanocrystals were precipitated with methanol and exchanged with pyridine. The samples were prepared by dropping a heavily concentrated solution of nanocrystals dispersed in pyridine onto silicon wafers. A slow evaporation of the pyridine leads to the formation of glassy thin films which were used for the diffraction experiments.

III. Results and Analysis

A. Synthesis of Core–Shell Composite Quantum Dots.

We use a two-step synthetic procedure similar to that of Danek et al.¹⁶ and Hines et al.¹⁹ to produce (CdSe)ZnS core–shell quantum dots. In the first step we synthesize nearly monodisperse CdSe nanocrystallites ranging in size from 23 to 55 Å via a high-temperature colloidal growth followed by size selective precipitation.³ These dots are referred to as “bare” dots in the remainder of the text, although their outermost surface is passivated with organic TOPO/TOP capping groups. Next, we overcoat the CdSe particles in TOPO by adding the Zn and S precursors at intermediate temperatures.²² The resulting composite particles are also passivated with TOPO/TOP on their outermost surface.

The temperature at which the dots are overcoated is very critical. At higher temperatures the CdSe seeds begin to grow via Ostwald ripening, and their size distribution deteriorates, leading to broader spectral line widths. Overcoating the particles at relatively low temperatures could lead to incomplete decomposition of the precursors or to reduced crystallinity of the ZnS shell. An ideal growth temperature is determined independently for each CdSe core size to ensure that the size distribution of the cores remains constant and that shells with a high degree of crystallinity are formed.²²

The concentration of the ZnS precursor solution and the rate at which it is added are also critical. Slow addition of the precursors at low concentrations ensures that most of the ZnS grows heterogeneously onto existing CdSe nuclei instead of undergoing homogeneous nucleation. This probably does not eliminate the formation of small ZnS particles completely so a final purification step in which the overcoated dots are subjected

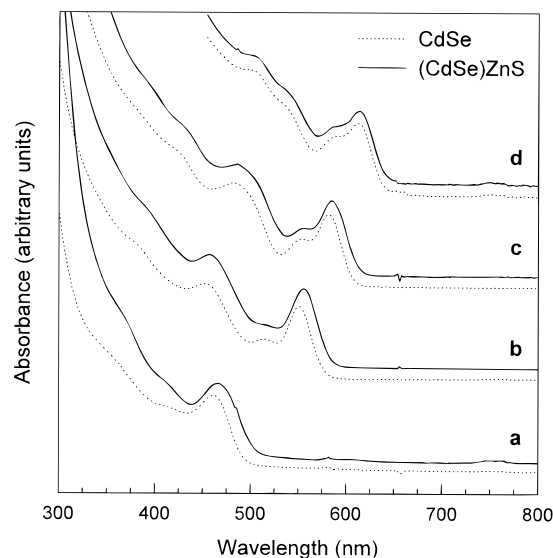


Figure 1. Absorption spectra for bare (dashed lines) and 1–2 monolayer ZnS overcoated (solid lines) CdSe dots with diameters measuring (a) 23, (b) 42, (c) 48, and (d) 55 Å. The absorption spectra for the (CdSe)ZnS dots are broader and slightly red-shifted from their respective bare dot spectra.

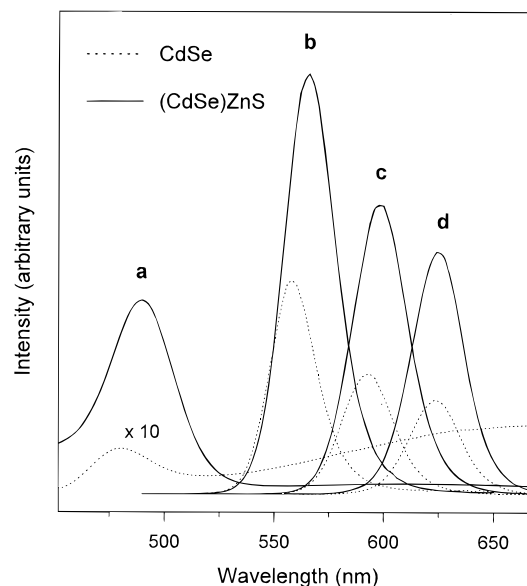


Figure 2. Photoluminescence (PL) spectra for bare (dashed lines) and ZnS overcoated (solid lines) dots with the following core sizes: (a) 23, (b) 42, (c) 48, and (d) 55 Å in diameter. The PL spectra for the overcoated dots are much more intense owing to their higher quantum yields: (a) 40, (b) 50, (c) 35, and (d) 30.

to size selective precipitation provides further assurance that mainly (CdSe)ZnS particles are present in the final powders.

B. Optical Characterization. The synthesis presented above produces ZnS overcoated dots with a range of core and shell sizes. Figure 1 shows the absorption spectra of CdSe dots ranging from 23 to 55 Å in diameter before (dashed lines) and after (solid lines) overcoating with 1–2 monolayers of ZnS. The definition of a monolayer here is a shell of ZnS that measures 3.1 Å (the distance between consecutive planes along the [002] axis in bulk wurtzite ZnS) along the major axis of the prolate-shaped dots. We observe a small shift in the absorption spectra to the red (lower energies) after overcoating due to partial leakage of the exciton into the ZnS matrix. This red shift is more pronounced in smaller dots where the leakage of the exciton into the ZnS shell has a more dramatic effect on the confinement energies of the charge carriers. Figure 2 shows the room-temperature photoluminescence spectra (PL) of these



Figure 3. Color photograph demonstrating the wide spectral range of bright fluorescence from different size samples of (CdSe)/ZnS. Their PL peaks occur at (going from left to right) 470, 480, 520, 560, 594, and 620 nm (quartz cuvettes courtesy of Spectrocell Inc., photography by F. Frankel).

same samples before (dashed lines) and after (solid lines) overcoating with ZnS. The PL quantum yield increases from 5 to 15% for bare dots to values ranging from 30 to 50% for dots passivated with ZnS. In smaller CdSe dots the surface-to-volume ratio is very high, and the PL for TOPO capped dots is dominated by broad deep trap emission due to incomplete surface passivation. Overcoating with ZnS suppresses deep trap emission by passivating most of the vacancies and trap sites on the crystallite surface, resulting in PL which is dominated by band-edge recombination.

Figure 3 (color photograph) displays the wide spectral range of luminescence from (CdSe)/ZnS composite quantum dots. The photograph shows six different samples of ZnS overcoated CdSe dots dispersed in dilute hexane solutions and placed in identical quartz cuvettes. The samples are irradiated with 365 nm ultraviolet light from a UV lamp in order to observe luminescence from all the solutions at once. As the size of the CdSe core increases, the color of the luminescence shows a continuous progression from blue through green, yellow, orange, to red. In the smallest sizes of TOPO capped dots the color of the PL is normally dominated by broad deep trap emission and appears as faint white light. After overcoating the samples with ZnS the deep trap emission is nearly eliminated, giving rise to intense blue band-edge fluorescence.

To understand the effect of ZnS passivation on the optical and structural properties of CdSe dots, we synthesized a large quantity of ~ 40 Å diameter CdSe dots. We divided this sample into multiple fractions and added varying amounts of Zn and S precursors to each fraction at identical temperatures and addition times. The result was a series of samples with similar CdSe cores but with varying ZnS shell thickness. Figure 4 shows the progression of the absorption spectrum for these samples with ZnS coverages of approximately 0 (bare TOPO capped CdSe), 0.65, 1.3, 2.6, and 5.3 monolayers. (See beginning of this section for definition of number of monolayers.) The spectra reflect a constant area under the lowest energy $1S_{3/2}-1S_e$ absorption peak (constant oscillator strength) for the samples with varying ZnS coverage. As the thickness of the ZnS shell increases, there is a shift in the $1S_{3/2}-1S_e$ absorption to the red,

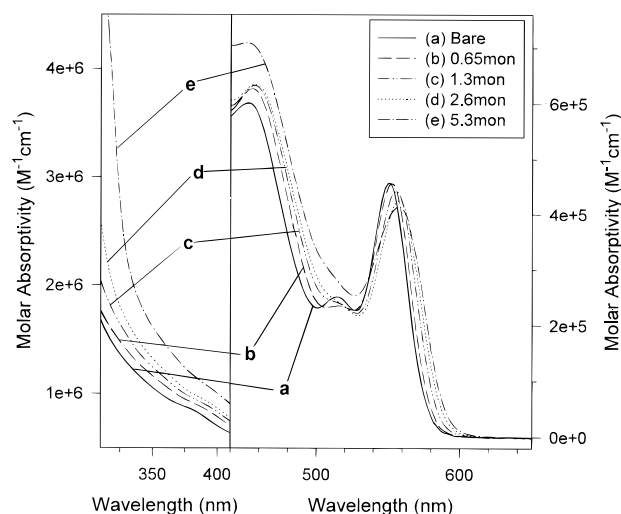


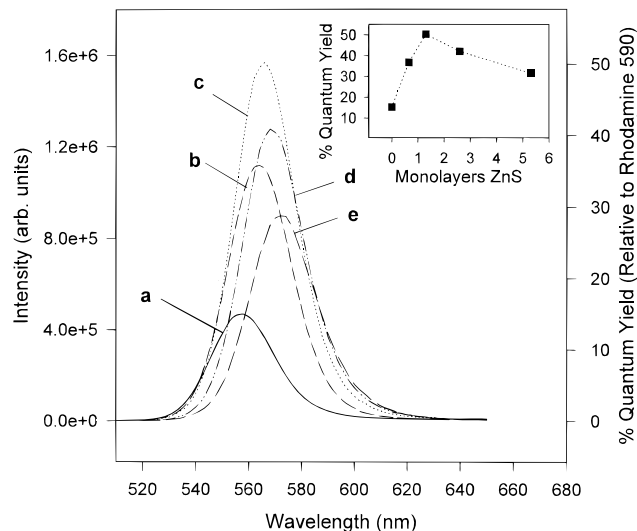
Figure 4. Absorption spectra for a series of ZnS overcoated samples grown on identical $42 \text{ Å} \pm 10\%$ CdSe seed particles. The samples displayed have the following coverage: (a) bare TOPO capped, (b) 0.65 monolayers, (c) 1.3 monolayers, (d) 2.6 monolayers, and (e) 5.3 monolayers (see definition for monolayers in text). The right-hand side shows the long wavelength region of the absorption spectra showing the lowest energy optical transitions. The spectra demonstrate an increased red-shift with thicker ZnS shells as well as a broadening of the first peak as a result of increased polydispersity. The left-hand side highlights the ultraviolet region of the spectra showing an increased absorption at higher energies with increasing coverage due to direct absorption into the ZnS shell.

reflecting an increased leakage of the exciton into the shell, as well as a broadening of the absorption peak, indicating a distribution of shell thickness. The left-hand side of Figure 4 shows an increased absorption in the ultraviolet with increasing ZnS coverage as a result of direct absorption into the higher band gap ZnS shell.

The evolution of the PL for the same ~ 40 Å diameter dots with ZnS coverage is displayed in Figure 5. As the coverage of ZnS on the CdSe surface increases, we see a dramatic increase in the fluorescence quantum yield followed by a steady decline

TABLE 1: Summary of the Results Obtained from WDS, TEM, SAXS, and WAXS Detailing the Zn/Cd Ratio, Average Size, Size Distribution, and Aspect Ratio for a Series of (CdSe)ZnS Samples with a ~ 40 Å Diameter CdSe Cores and Varying ZnS Coverage

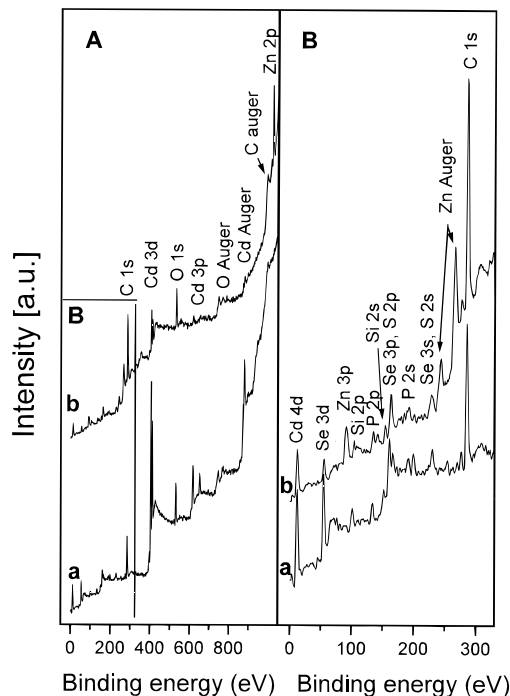
ZnS coverage (TEM)	measd TEM size	measd average aspect ratio	calcd size (SAXS in polymer)	measd Zn/Cd ratio (WDS)	calcd Zn/Cd ratio (SAXS in polymer)	calcd Zn/Cd ratio (WAXS)
bare	39 Å \pm 8.2%	1.12	42 Å \pm 10%			
0.65 monolayers	43 Å \pm 11%	1.16	46 Å \pm 13%	0.46	0.58	0.7
1.3 monolayers	47 Å \pm 10%	1.16	50 Å \pm 18%	1.50	1.32	1.4
2.6 monolayers	55 Å \pm 13%	1.23		3.60		2.9
5.3 monolayers	72 Å \pm 19%	1.23		6.80		6.8

**Figure 5.** PL spectra for a series of ZnS overcoated dots with $42 \pm 10\%$ Å diameter CdSe cores. The spectra are for (a) 0, (b) 0.65, (c) 1.3, (d) 2.6, and (e) 5.3 monolayers ZnS coverage. The position of the maximum in the PL spectrum shifts to the red, and the spectrum broadens with increasing ZnS coverage. (inset) The PL quantum yield is charted as a function of ZnS coverage. The PL intensity increases with the addition of ZnS reaching, 50% at ~ 1.3 monolayers, and then declines steadily at higher coverage. The line is simply a guide to the eye.

after ~ 1.3 monolayers of ZnS. The spectra are red-shifted (slightly more than the shift in the absorption spectra) and show an increased broadening at higher coverage. The inset to Figure 5 charts the evolution of the quantum yield for these dots as a function of the ZnS shell thickness. For this particular sample the quantum yield starts at 15% for the bare TOPO capped CdSe dots and increases with the addition of ZnS, approaching a maximum value of 50% at approximately ~ 1.3 monolayer coverage. At higher coverage the quantum yield begins to decrease steadily until it reaches a value of 30% at about ~ 5 monolayer coverage. In the following sections we explain the trends in PL quantum yield based on the structural characterization of ZnS overcoated samples.

C. Structural Characterization. Wavelength Dispersive X-ray Spectroscopy. We analyze the elemental composition of the ZnS overcoated samples using wavelength dispersive X-ray spectroscopy (WDS). This method provides a quantitative analysis of the elemental composition with an uncertainty of less than $\pm 5\%$. We focus on obtaining a Zn/Cd ratio for the ZnS overcoated samples of interest. Analysis of the series of samples with a ~ 40 Å diameter core and varying ZnS coverage gives the Zn/Cd ratios which appear in Table 1. The WDS analysis confirms that the Zn-to-Cd ratio in the composite dots increases as more ZnS is added. We also use this technique to measure the Se/Cd ratio in the bare dots. We consistently measure a Se/Cd ratio of ~ 0.8 – $0.9/1$, indicating Cd-rich nanoparticles.

X-ray Photoelectron Spectroscopy. Multiple samples of ~ 33 and ~ 40 Å diameter CdSe quantum dots overcoated with variable amounts of ZnS were examined by XPS. Figure 6

**Figure 6.** (A) Survey spectra of (a) ~ 40 Å diameter bare CdSe dots and (b) the same dots overcoated with ZnS showing the photoelectron and Auger transitions from the different elements present in the quantum dots. (B) Enlargement of the low-energy side of the survey spectra, emphasizing the transitions with low binding energy.

shows the survey spectra of ~ 40 Å diameter bare dots and of the same sample overcoated with ~ 1.3 monolayers of ZnS. The presence of C and O comes mainly from atmospheric contamination during the brief exposure of the samples to air (typically around 15 min). The positions of both C and O lines correspond to standard values for adsorbed species, showing the absence of significant charging.²⁴ As expected, we detect XPS lines from Zn and S in addition to the Cd and Se lines. Although the samples were exchanged with pyridine before the XPS measurements, small amounts of phosphorus could be detected on both the bare and ZnS overcoated CdSe dots, indicating the presence of residual TOPO/TOP molecules bound to Cd or Zn on the nanocrystal surfaces.²⁵ The relative concentrations of Cd and Se are calculated by dividing the area of the XPS lines by their respective sensitivity factors.²⁴ In the case of nanocrystals the sensitivity factor must be corrected by the integral $\int_0^d e^{-z/\lambda} dz$ to account for the similarity between the size of the nanocrystals and the escape depths of the electrons.²⁶ The integral must be evaluated over a sphere to obtain the Se/Cd ratios in CdSe dots. In the bare CdSe nanocrystals the Se/Cd ratio was around 0.87, corresponding to 46% Se and 54% Cd. This value agrees with the WDS results.

We use the Auger parameter, defined as the difference in binding energy between the photoelectron and Auger peaks, to identify the nature of the bond in the different samples.²⁴ This difference can be accurately determined because static charge corrections cancel. The Auger parameter of Cd in the bare and

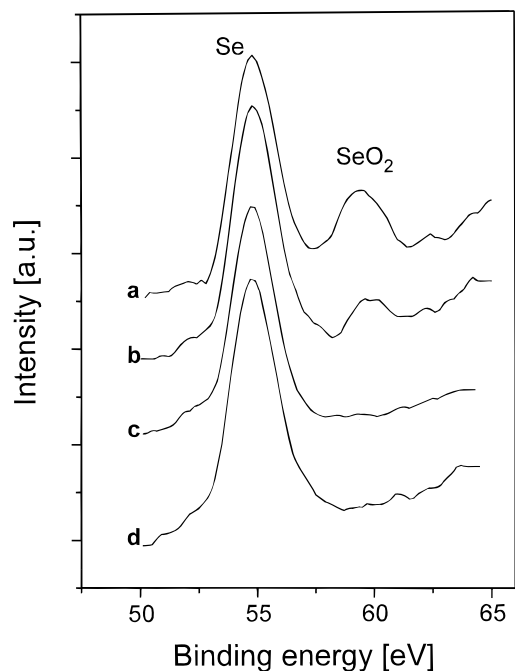


Figure 7. X-ray photoelectron spectra highlighting the Se 3d core transitions from ~ 40 Å bare and ZnS overcoated CdSe dots: (a) bare CdSe, (b) 0.65 monolayers, (c) 1.3 monolayers, and (d) 2.6 monolayers of ZnS. The peak at 59 eV indicates the formation of selenium oxide upon exposure to air when surface selenium atoms are exposed.

overcoated samples is 466.8 ± 0.2 eV and corresponds exactly to the expected value for bulk CdSe. In the case of ZnS the Auger parameter for Zn in the 1.3 and 2.6 monolayer ZnS samples is 757.5 eV, which is also very close to the expected value of 758.0 eV.

The degree of passivation of the CdSe surface with ZnS is examined by exposing the nanocrystal surface to air for extended periods of time and studying the evolution of the Se peak.

The oxidation of CdSe quantum dots leads to the formation of a selenium oxide peak at higher energies than the main Se peak.²⁷ Figure 7 shows the formation of a SeO_2 peak at 59 eV after an 80 h exposure to air in both the bare, TOPO capped, CdSe and 0.65 monolayer ZnS overcoated samples. These results indicate that in the 0.65 monolayer samples the ZnS shell does not completely surround the CdSe nanocrystals, and there are still Se sites at the surface that are susceptible to oxidation. In samples with an estimated coverage of ~ 1.3 monolayers ZnS or more the oxide peak does not appear even after prolonged exposure to air, indicating that the CdSe surface is possibly protected by a continuous ZnS shell. After exposure to air for 16 h, the bare CdSe nanocrystals display a selenium oxide peak which represents 13% of the total Se signal, and the Se/Cd ratio decreases to 0.77, corresponding to 43% Se and 57% Cd. The same sample after 80 h exposure to air had a ratio of Se/Cd of 0.37 (28% Se and 72% Cd), and the SeO_2 peak area was 22% of the total Se signal. For a ~ 40 Å diameter sample, 34% of the atoms are at the surface which means that in the sample measured most of the surface Se has been desorbed from the surface after 80 h. In the samples with more than 1.3 monolayers of ZnS coverage no change in the Se/Cd ratio was detected even after exposure to air for 80 h. Although no Cd-(O) peak appears after similar exposure to air, the Cd Auger parameter shifts from 466.8 eV for bare unoxidized CdSe to 467.5 eV for particles exposed to air for 80 h. The Auger parameter for the 1.3 and 2.6 monolayer coverage samples remains the same even after prolonged exposure to air.

Another method to probe the spatial location of the ZnS relative to the CdSe core is obtained by comparing the ratios

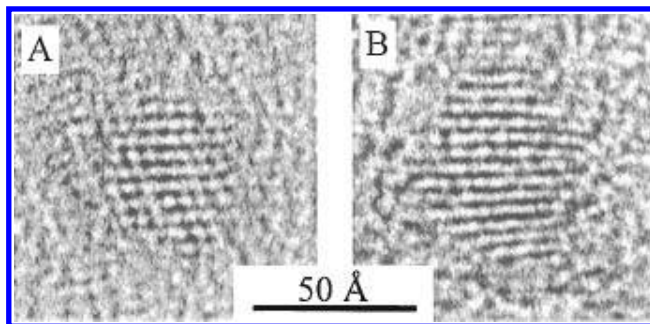


Figure 8. Transmission electron micrographs of (A) one "bare" CdSe nanocrystallite and (B) one CdSe nanocrystallite with a 2.6 monolayer ZnS shell.

of the XPS and Auger intensities of the Cd photoelectrons for bare and overcoated samples.^{14,28} The depth dependence of the observed intensity for the Auger and XPS photoemitted electrons is

$$I = J_0 N(z)_i \sigma_i Y_{i,n} F(KE) e^{-z/\lambda(KE)} \quad (1)$$

where J_0 is the X-ray flux, $N(z)_i$ is the number of i atoms, σ_i is the absorption cross section for atoms i , $Y_{i,n}$ is the emission quantum yield of Auger or XPS for atoms i , $F(KE)$ is the energy-dependent instrument response function, and $\lambda(KE)$ is the energy-dependent escape depth. Taking the ratio of the intensities of the XPS and Auger lines from the same atom, Cd or Zn, it is possible to eliminate the X-ray flux, number of atoms, and absorption cross sections from the intensity equations for the Auger and the primary X-ray photoelectrons. The value of the intensity ratio $I = i_{\text{overcoated}}(\text{Cd})/i_{\text{bare}}(\text{Cd})$, where $i = i_{\text{XPS}}(\text{Cd})/i_{\text{Auger}}(\text{Cd})$, is only a function of the relative escape depths of the electrons. Therefore, due to the smaller escape depths of the Cd Auger electrons in both ZnS (13.2 Å) and CdSe (10 Å) compared to the Cd XPS photoelectron (23.7 Å in ZnS and 15 Å in CdSe), the intensity I should increase with the amount of ZnS on the CdSe surface. Calculated values of 1.28 and 1.60 for the 0.65 and 2.6 monolayer, respectively, confirm the growth of ZnS on the surface of the CdSe dots.

Transmission Electron Microscopy. High-resolution TEM allows us to qualitatively probe the internal structure of the composite quantum dots and determine the average size, size distribution, and aspect ratio of overcoated particles as a function of ZnS coverage. We image the series of (CdSe)/ZnS samples described earlier. Figure 8 shows two dots from that series, one with (A) no ZnS overcoating (bare) and one with (B) 2.6 monolayers of ZnS. The particles in the micrographs show well-resolved lattice fringes with a measured lattice spacing in the bare dots similar to bulk CdSe. For the 2.6 monolayer sample these lattice fringes are continuous throughout the entire particle; the growth of the ZnS shell appears to be epitaxial. A well-defined interface between CdSe core and ZnS shell was not observed in any of the samples, although the "bending" of the lattice fringes in Figure 8B—the lower third of this particle is slightly askew compared with the upper part—may be suggestive of some sort of strain in the material. This bending is somewhat anomalous, however, as the lattice fringes in most particles were straight. Some patchy growth is observed for the highest coverage samples, giving rise to misshapen particles, but we do not observe discrete nucleation of tethered ZnS particles on the surface of existing CdSe particles. We analyze over 150 crystallites in each sample to obtain statistical values for the length of the major axis, the aspect ratio, and the distribution of lengths and aspect ratios for all the samples. Figure 9 shows histograms of size distributions and aspect ratio from these same samples. This figure shows the measured histograms for (A)

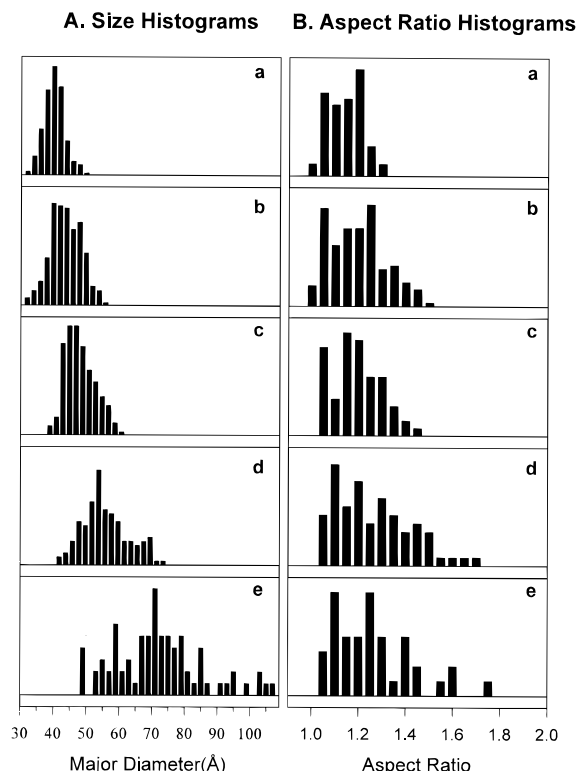


Figure 9. (A) Size histograms for the series of samples shown in Figure 8 measuring the longest dimension for over 150 particles in each sample. (B) Aspect ratio histograms for the same samples in (A) measured by taking the ratio of the major and minor axes for a subset of the particles analyzed. The samples measured are (a) bare dots, (b) 0.65 monolayers, (c) 1.3 monolayers, (d) 2.6 monolayers, and (e) 5.3 monolayers. The average values obtained appear in Table 1.

the major axis length and (B) the aspect ratio for 0, 0.65, 1.3, 2.6, and 5.3 monolayer coverage. The histograms clearly demonstrate an increase in the average length of the major axis from $39 \pm 8.2\%$ Å for bare dots to $72 \pm 19\%$ Å for the 5.3 monolayer ZnS overcoated dots as well as a broadening in the size distribution (see Table 1). The aspect ratio histograms demonstrate a larger distribution of aspect ratios and an overall increase in the aspect ratio with increasing coverage. The aspect ratio distributions are used to generate accurate fits to the small-angle X-ray scattering patterns. We use the values obtained from TEM throughout this paper to describe the thickness of the ZnS shell in terms of number of monolayers.

Small-Angle X-ray Scattering in Polymer Films. SAXS is a standard method used to size colloidal particles.^{29,30} The SAXS pattern for a collection of nearly monodisperse, noninteracting spheres displays a ringing pattern that is very sensitive to the size and size distribution of those objects. An increase in the size of these spheres shifts the peaks of the pattern to smaller angles, and an increase in the size distribution reduces the definition between peaks and valleys. A spectrum of the polymer matrix was subtracted from the raw data; that background-subtracted spectrum was then corrected for the fact that at very small angles the width of the X-ray beam exceeds that of the sample (generally 2 cm).³¹ Qualitative examination of the experimental scattering patterns (given by the dotted lines) in Figure 10 reveals a gradual shift of the ringing pattern to smaller angles as the thickness of the shell increases, indicating that ZnS is in fact growing onto the CdSe dots, instead of nucleating separate ZnS quantum dots. Also, for samples with a thin ZnS shell (0–1.3 monolayers), the SAXS patterns retain much of the structure present in the data for the bare particles, implying that lightly overcoating the dots preserves the initial size distribution of the CdSe core. On the other hand, patterns

for larger ZnS overlayers (>2.5 monolayers) contain few if any features, suggesting a large variation in the size and shape of the thicker shells. This behavior was seen for numerous other samples (with both smaller and larger CdSe cores) and appears to be a general feature of the overcoating procedure presented here.

To simulate the experimental data, we use a discrete form of the Debye equation,^{3,32}

$$I(q) = I_0 \left(\frac{f^2(q)}{q} \right) \sum_k \frac{\rho(r_k)}{r_k} \sin(qr_k) \quad (2)$$

where I_0 is the incident intensity, $f(q)$ is the angle-dependent scattering factor, and $q = [4\pi \sin \theta / \lambda]$, where θ is the angle of reflection and λ is the wavelength of the X-rays, $\rho(r_k)$ is the number of times a given distance r_k occurs, and the sum is over all interatomic distances. The position of the atoms in both the CdSe core and the ZnS shell are systematically generated in the wurtzite structure, and only those atoms falling inside the outlined ellipsoids are used for the simulation. The dimensions of the ellipsoids were taken from TEM measurements. To account for the shape distribution of the overcoated nanocrystallites, we weight the calculated patterns according to the aspect ratio histograms obtained from TEM (Table 1). We found that while the inclusion of a shape distribution for the overcoated particles generally had little effect on the final calculated pattern (i.e., the curve obtained for a 20 Å radius dot with an aspect ratio of 1.2 is quite similar to the sum of curves for 20 Å radius dots with aspect ratios of 1.1, 1.2, 1.3, and 1.4, which have been weighted 24, 36, 24, and 16%, respectively), such a distribution changes the calculated Zn/Cd ratio significantly. Fitting the experimental SAXS patterns of the overcoated quantum dots using particles of the same shape (aspect ratio) corresponds to a calculated Zn/Cd ratio much lower than that found by WDS. Use of a weighted distribution of shapes produces much better agreement between theoretically calculated and experimentally determined Zn/Cd ratios. With the aspect ratio of the particles dictated by TEM measurements, the size and size distribution of the ZnS shell were varied to fit the experimental SAXS data. The size, size distribution, and aspect ratio of the CdSe core were held constant in all calculations. For the sample series in Figure 10, only the curves of the bare CdSe, the 0.65 monolayer, and the 1.3 monolayer (CdSe)ZnS samples possessed enough structure to be fit confidently. Scattering patterns from samples with thicker ZnS shells (the 2.6 and 5.3 monolayers) were essentially featureless. Additional SAXS experiments confirmed that all nanocrystallites with ZnS shells larger than 3 monolayers had structureless experimental curves similar to the largest samples in Figure 10.

The shoulder at $2\theta < 2^\circ$ in the scattering patterns of the (CdSe)ZnS is seen in disordered thin films of CdSe (without a polymer matrix) and is indicative of aggregation of the dots.³³ This is reasonable behavior, probably due to the poor chemical passivation of the ZnS surface by TOPO, which we infer from empirical observations of the increased tendency of ZnS overcoated particles to irreversibly flocculate during repeated size-selective precipitation. We used the phosphine-functionalized diblock copolymer MTD₃₀₀P₂₀, known to provide increased passivation of CdSe quantum dots²³ in an attempt to prevent aggregation of the ZnS overcoated nanocrystallites. However, this was only slightly more effective than poly(vinyl butyral), which had been used for previous SAXS studies.³² Even preparing the polymer films in an inert atmosphere did not improve the separation of the particles. This aggregation makes the lower angle region ($< \sim 2.5^\circ$) of the data unreliable for fitting, but the calculated size is not affected, since the

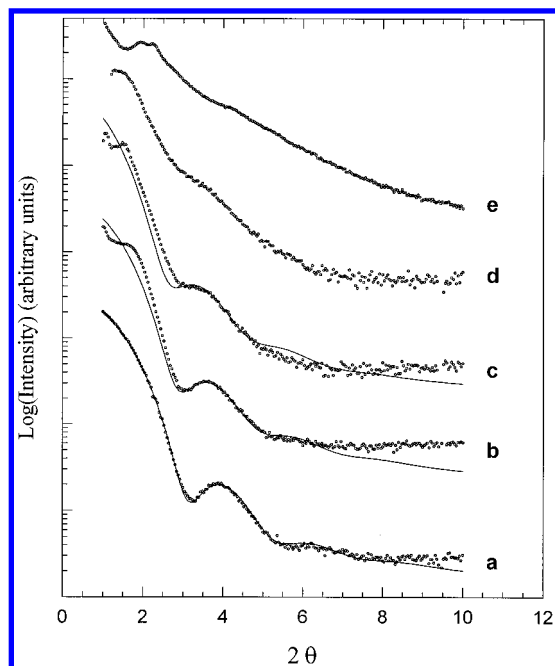


Figure 10. SAXS of bare and ZnS overcoated CdSe quantum dots dispersed in polymer films. Circles represent experimental data and lines the corresponding fits for lower coverage samples using the discrete form of the Debye equation. (a) Bare 42 Å diameter CdSe dots, (b) 0.65 monolayers, (c) 1.3 monolayers, (d) 2.6 monolayers, and (e) 5.3 monolayers.

position of the ringing pattern is not affected when the particles are close-packed.

Small-Angle X-ray Scattering from Dilute Solutions. In the case where the nanocrystallites are dispersed in solution, the scattered intensity with respect to the solvent background, caused by electronic density fluctuations in the medium, is a function of the electronic contrast between the solute objects (with density ρ_d) and the scattering background (with density ρ_s): $\Delta\rho = \rho - \rho_s$. Because large distances are scanned and dilute dispersions are used, the above intensity written as a discrete summation in eq 2 derives from the Fourier transform of the autocorrelation function of the electronic contrast, $\Delta\tilde{\rho}^2(r)$, and shows a strong dependence on the scattering objects size.^{29,30} In particular, the extrapolation to $q = 0$ provides the integral over the scattering volume V of the function $\Delta\tilde{\rho}^2(r)$ in real space and, thus, the total contrast of the scattering objects:

$$I(0) = \int_0^\infty 4\pi r^2 \Delta\tilde{\rho}^2(r) dr = N(v\langle\Delta\rho\rangle)^2 \approx NR^6 \quad (3)$$

where N is the number of particles in the scattering volume V , v is the particle specific volume, and R its radius. Equation 3 predicts a sixth-power dependence of the intensity on the radius, and a linear increase with N . In the present study, we focus primarily on the form factor, because only low concentrations are used. In addition, since our primary interest is an investigation of the effects of overcoating on the particle size, we use only dispersions that have comparable N . The total signal is proportional to the single-particle scattering $P_1(q,c)$: $I(q) \propto P(q,c) \approx NP_1(q)$. Examination of the strong power dependence of $I(0,N)$ on the radius is better done via the Guinier expression for the intensity $I(q,N) \approx I(0,N) \exp(-q^2 R_G^2/5)$, where R_G is the Guinier radius for spherical particles. A plot of $\ln(I)$ vs q^2 (Guinier plot) shows a linear behavior at intermediate to small q .

It is from the fit to the intensity over a wide range of q , except near $q = 0$, that we extract values for the average particle size R_0 and the polydispersity σ for the bare crystallites. This is done via Porod analysis where we plot $q^4 I(q)$ vs q . The latter

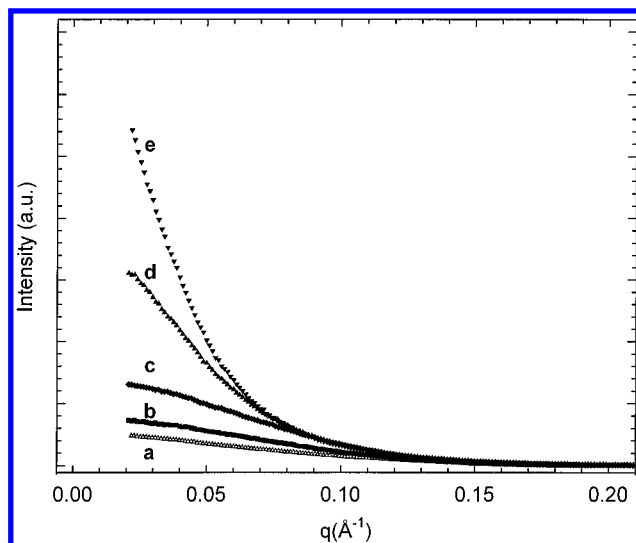


Figure 11. Scattered intensity, $I(q,c) = I_s(q,c) - I_{\text{ref}}(q,0)$, for bare and ZnS overcoated samples dispersed in hexane at a given concentration of particles per unit volume: (a) bare 42 Å diameter dots and (CdSe)ZnS with Zn/Cd ratios of (b) 0.42, (c) 0.85, (d) 3.1, and (e) 5.3.

starts from zero at the origin followed by a damped oscillating curve around a plateau that depends on the contrast. The periodicity of the curve depends on the size of the solute particles.^{29,30} The linearity of the experimental data in a Guinier diagram and the quality of the oscillations in a Porod diagram depend on the polydispersity of the scattering objects. We use either log-normal or Gaussian functions to describe the distributions of the particle size. Effects of the polydispersity, for example, translate into a reduction of the oscillations after the first peak in a Porod diagram. Polydispersity also translates into a departure from linear behavior in a Guinier plot. When polydispersity increases, the oscillations characteristic of a single sphere form factor merge into a diffuse decaying curve in a $\ln(I)$ vs q plot.^{29,30}

Figure 11 shows SAXS spectra ($I = I_s - I_{\text{ref}}$) for a series of samples with a ~ 40 Å diameter CdSe core and different amounts of ZnS coverage at a fixed concentration (Note: these samples have different Zn to Cd ratios than the samples used in the remainder of this paper and therefore are not compared directly with the other measurements in Table 1). The above spectra show a classic behavior, with a large contribution to the signal from the solute crystallites at small angles and a decrease to zero at large q . In addition, the scattered intensity, $I(q)$, strongly increases with increasing ZnS coverage. This is in agreement with the predictions of eq 3, since an increase of the overall particle size is expected with increasing ZnS coverage.

In Figure 12A, we show Guinier plots ($\ln(I)$ vs q^2) for the dispersions of overcoated dots with Zn/Cd ratios of (b) 0.42/1, (c) 0.85/1, (d) 3.1/1, and (e) 5.6/1. The data for the crystallites with low Zn/Cd ratios (b, c) show a linear dependence of $\ln(I)$ vs q^2 as expected from eq 2. However, the data for the higher coverage (d, e) samples do not show a linear behavior. A progressive convex curvature appears at large angles and persists as q decreases to 0. This curvature can be simulated using a relatively large size distribution. Attractive interparticle interactions could also lead to similar behavior.³⁴ Because of the long-term stability of the dispersions in dilute solution, we choose to attribute the above peculiar behavior of the experimental Guinier diagrams to an increase in the polydispersity of the heavily overcoated (CdSe)ZnS particles.

In Figure 12B, we show Porod plots, $q^4 I(q)$ vs q , for the different dispersions. The data for (a) bare and Zn/Cd ratios of (b) 0.42 and (c) 0.85 showed behavior similar to classical dispersions, with zero value at $q = 0$, followed by a few

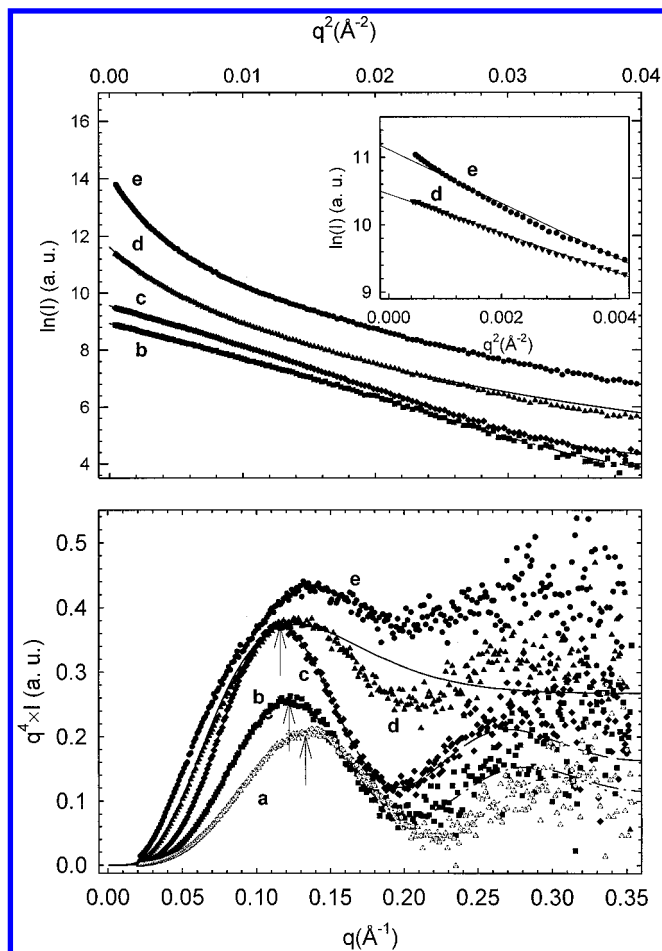


Figure 12. (top) Guinier plots for the same dispersions as in Figure 11. A linear dependence of $\ln(I)$ vs q^2 is shown with the lower coverage samples (b, c). Continuous curvature (departure from the linear behavior) is observed for the higher coverage. The inset shows the data for samples (d, e) over a small range of q , close to the origin. (bottom) Porod plots for the same dispersions shown in Figure 11. The arrows indicate a decreasing q_M with increasing size. Samples a–c show clear oscillations similar to the behavior of classical dispersions. The data from the higher coverage samples d and e show more scattering and loss of the oscillations as a result of larger polydispersities in size and shape. The curves are fits to the data with $\sigma = 0.11$ (a), 0.14 (b), 0.16 (c), and 0.25 (d).

oscillations (~ 1 – 2). Furthermore, the position of q_{Max} decreases with increasing coverage, reflecting an increase of the particle size. The data for the dispersion (a) in hexane can be fit to an intensity generated by a set of polydisperse noninteracting spheres over a wide range of q , but far enough from the origin, with $R_0 \approx 19.50$ Å and $\sigma \approx 0.12$. These values are in agreement with previous SAXS measurements on similar crystallites (with similar absorption peak positions), submitted to comparable size selection.³⁴ Discarding the region close to the origin in the fit reduces effects of the interactions. Also, a fit using Porod analysis provides more accurate estimates for the size and the polydispersity, since a fit to a peak is involved. The data for the two other dispersions (b, c) can also be fit with a set of polydisperse particles. The sizes increase as expected, but so does the polydispersity. However, for samples with higher Zn/Cd ratios (d) 3.1, (e) 5.3, the oscillations at large q are reduced. The corresponding data could not be fit with reasonable σ , as expected from the appearance of a plateau in the Porod plots. The large polydispersity may be associated with an increase in size as well as shape distributions, as shown in the TEM data. This problem makes the data analysis and extraction of estimates for size and variance meaningless. Because of this, we choose to extract the largest size in the

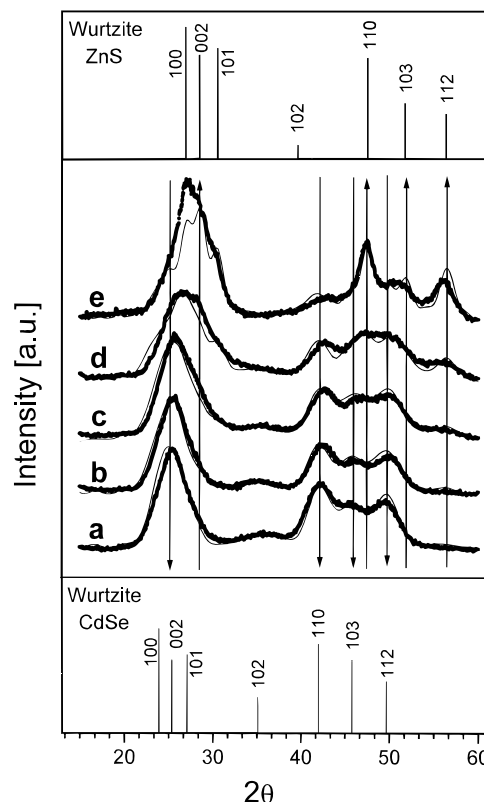


Figure 13. WAXS patterns for (a) ~ 40 Å diameter bare CdSe nanocrystals and ZnS overcoated samples with coverages of (b) 0.65, (c) 1.3, (d) 2.6, and (e) 5.3 monolayers. Circles represent the experimental data while solid lines show the fits to the ellipsoidal model detailed in the text. The Zn/Cd ratios used in the simulations are comparable to the WDS measurements. The powder patterns for wurtzite CdSe and ZnS are shown for comparison in the bottom and top insets, respectively.

distribution rather than an average. These sizes are derived from the power dependence of the intensity with size, using eq 3. From the Guinier plots in Figure 12A, we extract a value for $I(0)$ from extrapolation of the linear curve for all samples. The sizes are derived from $R \approx R_{0m}[I_{nm}(0)/I_{0m}(0)]^{1/6}$. For the dispersions (b, c), where polydispersity is still relatively small, extrapolation of I to $q = 0$ is straightforward. However, for the larger coverage (d, e), where polydispersity becomes important, we must limit the extrapolation from a smaller region near $q = 0$, since only the upper bracket in the distribution (upper size) is of interest in this case.

In the above fits, we consider a single electron density for the CdSe core and the ZnS thin shell. This is not correct since the elements involved in the dot structure have different characteristics: $\rho(\text{CdSe}) \approx 2.92$ e/Å³ and $\rho(\text{ZnS}) \approx 2.35$ e/Å³. This assumption implies an error of about 10–15% in the above size estimates. This should not seriously affect the final result, since values for the upper limit in the size distribution are extracted for samples with high coverage, and the shell contribution to the CdSe core for the lower coverage is very small. The effects of the above assumption are further reduced by the fact that the two densities are much larger than the solvent background. The values for the effective radii obtained from this analysis follow the same general trend as the data obtained by the other techniques indicating once more that the ZnS is growing directly onto the CdSe core.

Wide-Angle X-ray Scattering. WAXS probes the internal structure of (CdSe)ZnS and provides information about the lattice parameters of the core and shell. Figure 13 displays diffraction patterns for ~ 40 Å diameter CdSe particles overcoated with different amounts of ZnS as indicated previously.

The experimental WAXS patterns of the composite dots (solid circles) consist of rather broad features that do not match with the bulk wurtzite CdSe or wurtzite ZnS lines. Spectrum a corresponds to the bare CdSe nanocrystals used as nucleation centers for the ZnS growth. The first broad feature is a convolution of the (100), (002), and (101) reflections and is indicative of the finite size of the sample. The decrease in the intensity of the (102) and (103) peaks compared to the powder pattern of the bulk material is caused by the presence of stacking faults along the [002] direction.³ The X-ray diffraction patterns of composite nanocrystals with ZnS coverage ranging from (b) 0.65 to (e) 5.3 monolayers show a strong influence of the ZnS shell on the overall diffraction pattern. The solid lines in spectra a–e correspond to the calculated powder patterns. Again, we use eq 2 to simulate the wide angle region ($15^\circ < \theta < 60^\circ$). The simulation includes the effects of stacking fault density, thermal fluctuations, aspect ratio, and size distribution.^{2,3}

The experimental pattern of the bare dots is simulated using an average stacking fault density of 1.4 per crystallite and prolate particles containing ~ 1200 atoms with an aspect ratio of 1.1. These parameters are kept constant for the CdSe core in all other simulations. The following features can be outlined from Figure 13: a broadening and shift to higher angles of the first convolution feature initially located around 26° , a decrease in the intensity of the (102) CdSe line at 36° , a change in the position and relative intensities of the three peaks around 47° , and at high ZnS coverage (spectra d and e) the appearance of a new peak at 56° .

A glance at the powder patterns for wurtzite CdSe and ZnS (bottom and top insets in Figure 13) shows that the X-ray patterns of the composite particles may be fit by adding the weighted contributions to the scattering from both structures. To understand the structure of the composite particles, we perform detailed simulations probing the effect of the ZnS shell on the WAXS patterns. The scattering factors of ZnS are smaller than those of CdSe, leading to weaker contributions to the overall X-ray spectrum. We estimate that the integrated area of the first convolution feature in ZnS is a factor of 3 smaller than for CdSe. Thus, the presence of large amounts of ZnS is necessary to resolve its structure in the X-ray pattern, as is the case for the samples with 2.6 and 5.3 monolayers of ZnS (Figure 13d,e). All the features mentioned above can be simulated by introducing ZnS shells of different thickness on the CdSe core. However, to obtain reasonable agreement between experimental and simulated patterns for heavier coverage (2.6 and 5.3 monolayers), the lattice parameters of both structures must be set to their respective bulk values, $a_{\text{CdSe}} = 4.29 \text{ \AA}$ and $a_{\text{ZnS}} = 3.82 \text{ \AA}$. In the case of samples with a small coverage of ZnS (0.65 and 1.3 monolayers) (Figure 13b,c) the choice for the lattice parameter of ZnS had little effect on the fits to the X-ray scattering patterns.

Average size measurements and shape determinations from TEM define the dimensions of the ellipsoids in the simulations. While the aspect ratio for CdSe is 1.15, the value for the ZnS shell is weighted between 1.2 and 1.4 based on TEM measurements (Table 1). At larger coverage most of the particles are elongated along the [002] axis, and therefore the distribution of shapes is weighted toward the larger numbers.

An interesting point revealed by the simulations is the presence of stacking faults (SF) along the [002] direction in the ZnS overlayer. The importance of the SF density is apparent in the simulated spectrum for the sample with the highest Zn/Cd ratio. The best fit occurs when an average of three SF per crystallite is included in the ZnS shell. Note that to fit the other spectra there is no need to include stacking faults because the thickness of the ZnS shell is at most 1–2.5 monolayers, and its

contribution to the overall X-ray signal is small. [Zn/Cd] ratios of 0.7, 1.4, 2.9, and 6.8 were used to obtain the best fits. These values are close to those obtained by WDS (Table 1), supporting the validity of our simulations. The difference in the first broad diffraction peak between simulated and experimental profiles in spectrum e of Figure 13 suggests a possible change in orientation between the core and overlayer. However, rotating the overlayer to match the (100) planes of the ZnS structure to the (101) planes of the CdSe nanocrystal did not improve the fit significantly.

One added problem comes from the difference in lattice parameters between the two materials which affects the matching of the interfaces. The summation in eq 2 has to be performed over all the distances, and consequently it may take into account interactions among all the atoms in the composite structure, whether or not they belong to the same phase, provided that the atoms are not too far away from each other. Thus, the atomic positions at the interface may need to be modeled accurately. To determine the importance of this interaction on the X-ray profiles, we carried out simulations with and without interactions between CdSe and ZnS. In the case of no interaction one only needs to add the X-ray scattering factors from the ZnS shell to the factors for the CdSe core. In the other case, the cross terms (I_{CdS} , I_{ZnSe} , I_{SSe} , I_{CdZn}) in eq 2 need to be considered. Although small modifications exist in the X-ray pattern (mainly in the first diffraction feature), the difference between the noninteracting and the interacting case is much less significant than the effect of changing the Zn/Cd ratio, the aspect ratio, or the stacking fault density in the patterns.

IV. Discussion

After successfully producing (CdSe)/ZnS dots with a wide range of core sizes, we focus our attention on one particular sample of CdSe seeds and study the evolution of the optical and structural properties as a function of ZnS coverage. We first use a simplified theoretical approach to model the shifts in energy with increasing shell thickness for CdSe dots overcoated with different amounts of ZnS or CdS. We then proceed to analyze the structure of (CdSe)/ZnS composite dots with varying amounts of ZnS in order to determine how the structure of these dots influences their fluorescence. Finally, we attempt to characterize the growth mechanism for the ZnS shell onto the CdSe core.

A. Theoretical Modeling of the Electronic Structure. We use a simplified model of noninteracting particles in a spherical box to describe the electron and hole wave functions and confinement energies inside the composite quantum dots.^{13,35,36} The objective here is to understand the trends in red shifts in absorbance with increasing ZnS coverage, the difference in red shifts between ZnS and CdS overcoats, and the difference in red shifts in absorption and emission.

We assume the dots consist of a spherical CdSe core surrounded by a concentric shell of ZnS and that there is no alloying at the interface. We assign a potential energy of zero inside the CdSe core and a barrier height of 0.9 eV for both the electron and hole to tunnel into the ZnS shell.³⁷ In this picture the electron (hole) must tunnel through a 4 eV (10 eV) barrier to extend into the surrounding organic matrix. The Coulomb attraction between the electron and hole is treated in first-order perturbation theory. We obtain the solutions for the composite particles by solving the continuity relations for the electron and hole wave functions, eq 4, and the probability currents, eq 5, at the CdSe/ZnS interface:

$$R_{1\text{S,CdSe}}(k_1 r_1) = R_{1\text{S,ZnS}}(\kappa_2 r_1) \quad (4)$$

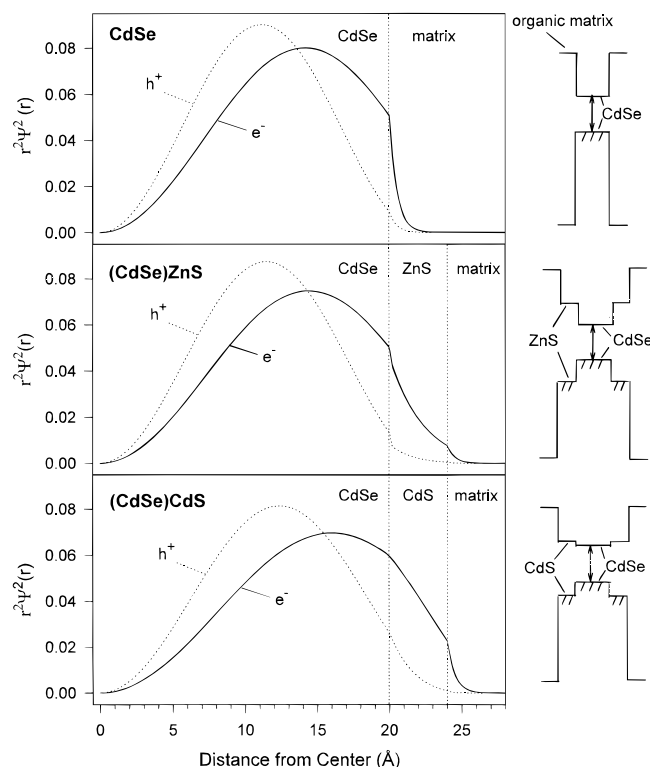


Figure 14. Radial probability functions for the lowest energy ($1S_{3/2}-1S_e$) electron and hole wave functions in (A) bare 20 Å diameter CdSe dots, (B) (CdSe)ZnS dots with a 20 Å diameter core and a 4 Å ZnS shell, and (C) (CdSe)CdS dots with an identical core and a 4 Å CdS shell. The sketches to the right show the approximate band offsets between the various components.

$$\frac{1}{m_{\text{CdSe}}^*} \frac{d}{dr} R_{1S, \text{CdSe}}(k_1 r)|_{r=r_1} = \frac{1}{m_{\text{ZnS}}^*} \frac{d}{dr} R_{1S, \text{ZnS}}(k_2 r)|_{r=r_1} \quad (5)$$

where $R_{1S, \text{CdSe}}$ and $R_{1S, \text{ZnS}}$ are the lowest energy radial wave functions for the electron or hole in the CdSe core and ZnS shell, respectively, r_1 is the radius of the CdSe core, m_{CdSe}^* and m_{ZnS}^* represent the hole or electron bulk effective masses in CdSe and ZnS, respectively, and k_1 and k_2 are the wave vectors in CdSe and ZnS, respectively.

Figure 14 shows the radial probabilities of the electron and hole in the lowest energy $1S_{3/2}-1S_e$ eigenstates for bare (TOPO capped) ~ 20 Å radius CdSe dots (a) and for the same dots with a 4 Å ZnS (b) or 4 Å CdS (c) shell. In the bare dots the wave function of the lighter electron spreads over the entire particle and tunnels only slightly into the surrounding organic matrix whereas the heavier hole has a higher probability at the center of the dot and does not extend into the surrounding matrix. When a shell of ZnS surrounds the CdSe particle, the electron wave function tunnels into the ZnS shell while the hole wave function has a negligible probability of spreading into the ZnS layer. The increased delocalization of the electron lowers its confinement energy and consequently the energy of the excited state. Beyond a certain thickness of the ZnS shell the electron and hole wave functions cannot spread out further, and the confinement energies remain constant.

In CdS the barrier height for the electron (0.2 eV) is smaller than the total energy of the electron, and thus its wave function extends well into the CdS shell. The hole, however, must tunnel through a 0.55 eV barrier into the CdS shell and therefore has lower probability of penetrating into the surrounding CdS matrix than the electron but extends into the CdS more than it does for a ZnS shell.

We estimate the energy shift as a function of ZnS shell thickness for a series of samples grown on ~ 20 Å radius CdSe

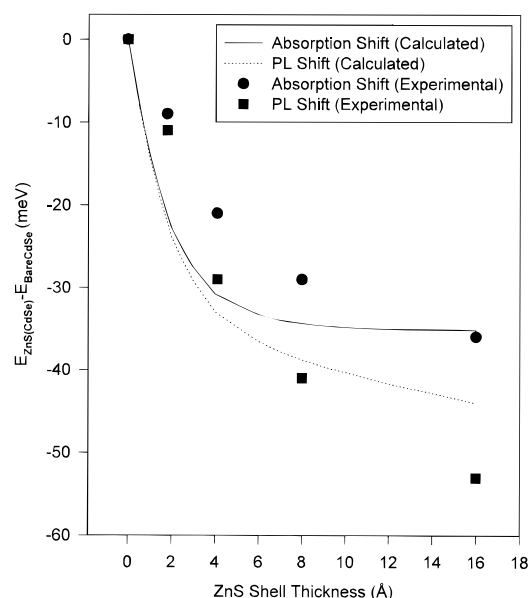


Figure 15. Energy difference between bare ~ 20 Å radius CdSe and (CdSe)ZnS particles as a function of ZnS shell thickness. The experimentally measured shifts in the first absorption feature appear as solid circles. The shifts in PL appear as solid squares. The calculated energy shifts for the absorption are plotted (solid line) vs shell thickness. The calculated shifts in the positions of the PL peaks are represented by the dashed lines.

dots. Figure 15 shows the experimental measurements (solid circles) of the difference in energy for the lowest energy $1S_{3/2}-1S_e$ transition between bare and ZnS overcoated dots as a function of the ZnS shell thickness. The solid line represents the calculated values using a 4 eV barrier for the electron to tunnel into the organic matrix and a 10 eV barrier for the hole. These values generated the best fit to the experimental data but should not be taken literally since they are essentially fitting parameters which in addition to modeling the real difference in band offsets also account for general deficiencies in this simplified model. The solid squares show the difference in energy between the PL peaks (excitation at 450 nm) for bare and overcoated samples. The dashed line represents the calculated values for the shift in PL vs shell thickness. The shifts in PL are larger than the shifts in absorption with the discrepancy increasing at higher ZnS coverage. Most of the increase in the shift can be accounted for by the increased size distribution in the samples with higher coverage. A partial dependence of the nonresonant Stokes shift on the size distribution has already been demonstrated for bare (organically passivated) CdSe dots.²⁵ The increased shift is the result of preferential absorption into the largest dots in the size distribution at the excitation wavelength (100 nm to the blue of the first absorption feature) leading to a larger red-shift for broader size distributions.³⁸ The experimental values for the shifts in absorption and PL appear to be in agreement with the values obtained by simple theoretical modeling.

Figure 16 shows the energy difference between bare and CdS overcoated ~ 30 Å radius CdSe dots as a function of CdS shell thickness. The shift in the exciton energy as a function of CdS coverage is much larger than it was in the case of ZnS. This effect is not surprising since the introduction of a CdS shell lowers the electron confinement energies to a greater extent than in the ZnS shell. The measured values are shown as solid circles with the error bars reflecting the size distributions from TEM. The calculated values for the shifts are represented by the solid line.

The largest shift in the first absorption feature for ~ 20 Å radius dots obtained for a 16 Å thick shell of ZnS is ap-

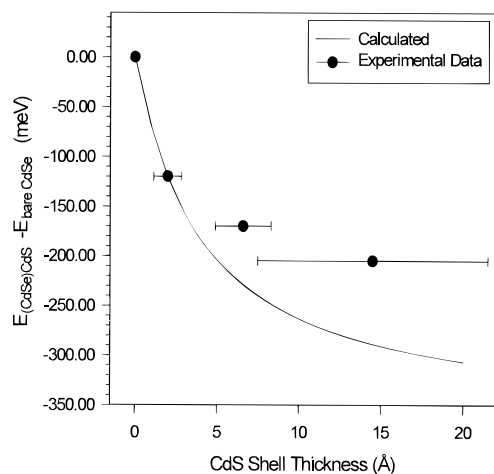


Figure 16. Energy difference between bare ~ 16 Å radius CdSe and (CdSe)CdS particles as a function of the CdS shell thickness. The experimental data appear as solid circles with error bars representing the size distribution obtained from TEM measurements. The estimated energy shifts for these particles assuming a 4 eV (10 eV) barrier for the electron (hole) to tunnel into the surrounding CdS matrix are shown for comparison (solid line).

proximately 36 meV. The shift for a 16 Å shell of CdSe on top of the same ~ 20 Å radius particles would be almost an order of magnitude higher (290 meV). In the CdS overcoated particles the shift for a 15 Å shell of CdS deposited onto ~ 16 Å radius CdSe dots was ~ 210 meV. Depositing a 15 Å shell of CdSe onto these same particles instead of CdS would result in a ~ 390 meV shift.

B. Characterization of ZnS Shell and Its Influence on PL Quantum Yield. Table 1 summarizes the structural information obtained from WDS, TEM, SAXS, and WAXS which includes values for the average size, size distribution, and Zn/Cd ratios obtained for the series of (CdSe)ZnS samples with a ~ 40 Å diameter core. The close agreement among the different methods lends credibility to the analysis and allows us to describe the structure of the composite dots with greater confidence.

Referring back to the inset of Figure 5, two important features stand out: a maximum efficiency of 50% at ~ 1.3 monolayer coverage and a steady decrease in the quantum yield beyond that point with increasing ZnS coverage.

The first feature is explained by the results of XPS analysis. The absence of a SeO_2 peak after exposure to air for 80 h is evidence that the majority of surface Se sites are passivated by an inorganic ZnS shell. The first sample in this series where surface oxidation is absent is one with approximately 1.3 monolayer coverage according to TEM and SAXS. The PL quantum yield reaches its maximum value at this same coverage indicating that most of the surface vacancies and nonradiative recombination sites are passivated.

We now focus our attention on understanding the growth of thicker ZnS shells and how that leads to a decline in the PL quantum yield. Detailed structural analysis via TEM on the higher coverage ZnS overcoated dots reveals slightly nonuniform growth of the ZnS shell and preferential growth in the [002] wurtzite direction of the CdSe core. This results in slightly elongated and in some cases irregularly shaped dots. These samples are also much more prone to irreversible flocculation than dots with lower ZnS coverage, indicating poor coordination of the TOPO capping groups to the surface Zn atoms.

To simulate the WAXS patterns for the highest coverage of ZnS on the CdSe cores, it was necessary to use the bulk lattice parameters for CdSe and ZnS. Furthermore, we included on average three stacking faults per crystallite along the [002]

direction in the ZnS shell to fit the experimental profiles. The presence of stacking faults along the [002] direction in these types of structures is due to their low energy of formation,³⁹ leading to preferential growth along that direction. This results in elongated particles with aspect ratios close to 1.3 and 1.4 as determined from TEM and SAXS. Defects in the ZnS shell may be the source of new nonradiative recombination sites and thus lead to a decline in the quantum yield of composite particles with thick ZnS shells.

Finally, we speculate as to the mechanism by which ZnS grows on top of the existing CdSe seed particles. Excluding the presence of separate ZnS particles, the growth of ZnS on the CdSe nanocrystals may be described one of three ways: coherent epitaxial with a large distortion or strain, incoherent epitaxial (with dislocations), or highly disordered.

The presence of a highly disordered ZnS shell can be eliminated because the X-ray diffraction peaks clearly originate from a crystalline structure. The other two possibilities are more difficult to differentiate. The initial growth of ZnS on the surface of CdSe is hard to characterize from the data available. The WAXS patterns for the low-coverage samples are dominated by scattering from the heavier Cd and Se atoms, so very little information can be derived from the ZnS shell. TEM studies show that lattice planes extend straight across particles, with no evidence of an interface, consistent with a coherent epitaxial mechanism for the growth. However, at a coverage higher than ~ 2 monolayers, WAXS studies indicate that the ZnS shell grows with the bulk lattice parameter, indicating an incoherence between the core and the shell. In this case TEM and WAXS are complementary. The nanocrystallites in the TEM micrographs appear to have an epitaxial ZnS shell, but the resolution was not sufficient to measure a difference between core and shell lattice fringe spacings, and dislocations or defects in a plane other than that in the micrograph cannot be observed. WAXS patterns clearly show that the ZnS shell has its own lattice parameter, but simulated spectra were insensitive to the orientation of that shell. Using the information from these two techniques, we describe the thicker overlayers as epitaxial but incoherent.

Regarding the actual mechanism of ZnS shell growth, there are two likely scenarios. The first and most likely possibility given the TEM and WAXS data is that the growth could initially be coherent at low coverage, but as the thickness of the shell increases, the strain due to the lattice mismatch (12%) between CdSe and ZnS could lead to the formation of dislocations and low-angle grain boundaries, relaxing the structure and causing the growth to proceed incoherently. These defects could be the source of nonradiative recombination sites within the ZnS overlayer. This behavior has already been reported for ultrathin CdSe/ZnSe quantum wells where the lattice misfit between subsequent layers is only 7%.⁴⁰ In this case, the reduction in the PL intensity was attributed to the generation of misfit dislocations when the thickness of the CdSe layer exceeded 4 monolayers.

Another possibility is that the growth begins with a large density of nucleation sites producing many, small islandlike clusters of ZnS with a structure locally coherent with the core. These islands then coalesce as the thickness of the shell increases to form a continuous film on the CdSe surface with a structure that has relaxed at the outer boundary to that bulk ZnS. The formation of grain boundaries as the islands coalesce could then be the origin of nonradiative recombination sites. In either case particles with very high ZnS coverage would have the bulk ZnS lattice parameter, and their quantum yield would decrease with increasing ZnS coverage as is observed in these samples.

V. Conclusion

A synthetic procedure for the production of core-shell quantum dots whose emission spans most of the visible spectrum is described. These samples are analyzed optically and structurally using numerous techniques. TEM, SAXS, and WDS demonstrate an increase in the size of the composite particles with increasing Zn/Cd ratio as well as an increase in the size distribution and aspect ratio. WAXS is used to probe the internal structure of the dots and indicates that at very high coverage the ZnS shell retains its bulk lattice parameter. The ZnS shell appears to be epitaxial and coherent at low coverage. At higher coverage the growth is probably epitaxial but incoherent as dislocations or other defects are created to accommodate the mismatch in lattice constants between ZnS and CdSe.

The influence of surface passivation on the optical properties is also evaluated. We explain the shifts in absorption and emission as a function of coverage using a simple theory treating the charge carriers as particles in a spherical box. We find that the quantum yield of ZnS overcoated samples reaches a maximum value shortly after ~ 1.3 monolayers of ZnS is added. At this coverage XPS measurements indicate that most of the surface Se sites are coordinated. The decrease in quantum yield at higher coverage is attributed to the formation of defects in the ZnS shell.

Acknowledgment. We thank Ken Kuno and Dr. Manoj Nirmal for stimulating discussions, Dr. Neel Chatterjee for the WDS measurements, and Felice Frankel for the photography. B.O.D., J.R.V., F.V.M., and J.R.H. acknowledge fellowships from Saudi Aramco, the Direccio General de Recerca from Catalonia, NSF, and DoD, respectively. M.G.B. thanks the David and Lucille Packard Foundation, the Sloan Foundation, and the W. M. Keck Foundation for funding. This research was funded in part by NSF Grant DMR-91-57491 and by the NSF-MRSEC program (DMR-94-00034). This research made use of the facilities of the MIT Center for Materials Science and Engineering funded through the NSF-MRSEC program (DMR-94-00034).

References and Notes

- (1) For recent reviews see for example: Brus, L. E. *Appl. Phys. A* **1991**, 53, 465. Alivisatos, A. P. *J. Phys. Chem.* **1996**, 100, 13226. Weller, H. *Adv. Mater.* **1993**, 5, 88. Bawendi, M. G.; Steigerwald, M. L.; Brus, L. E. *Annu. Rev. Phys. Chem.* **1990**, 41, 477.
- (2) Bawendi, M. G.; Kortan, A. R.; Steigerwald, M. L.; Brus, L. E. *J. Chem. Phys.* **1989**, 91, 7282.
- (3) Murray, C. B.; Norris, D. J.; and Bawendi, M. G. *J. Am. Chem. Soc.* **1993**, 115, 8706.
- (4) Chemsiddine, A.; Weller, H. *Ber. Bunsen-Ges. Phys. Chem.* **1993**, 97, 636.
- (5) Micic, O. I.; Sprague, J. R.; Curtis, C. J.; Jones, K. M.; Machol, J. L.; Nozik, A. J.; Giessen, H.; Fluegel, B.; Mohs, G.; Peyghambarian, N. *J. Phys. Chem.* **1995**, 99, 7754.
- (6) Ekimov, A. I.; Hache, F.; Schanne-Klein, M. C.; Ricard, D.; Flytzanis, C.; Kudriatsev, I. A.; Yazeva, T. V.; Rodina, A. V.; Efros, A. L. *J. Opt. Soc. Am. B* **1993**, 10, 100.
- (7) Alivisatos, A. P.; Harris, A. L.; Levinos, N. J.; Steigerwald, M. L.; Brus, L. E. *J. Chem. Phys.* **1988**, 89, 3435.
- (8) Nirmal, M.; Murray, C. B.; Bawendi, M. G. *Phys. Rev. B* **1994**, 50, 2293.
- (9) Chamorro, M.; Gourdon, C.; Lavallard, P.; Ekimov, A. I. *Jpn. J. Appl. Phys.* **1995** (Suppl. 34-1), 12.
- (10) Efros, A. L.; Rosen, M.; Kuno, M.; Nirmal, M.; Norris, D. J.; Bawendi, M. G. *Phys. Rev. B* **1996**, 54, 4843.
- (11) Norris, D. J.; Bawendi, M. G. *Phys. Rev. B* **1996**, 53, 16338.
- (12) Tian, Y.; Newton, T.; Kotov, N. A.; Guldi, D. M.; Fendler, J. J. *Chem. Phys.* **1996**, 100, 8927.
- (13) Youn, H. C.; Baral, S.; Fendler, J. H. *J. Phys. Chem.* **1988**, 92, 6320.
- (14) Kortan, A. R.; Hull, R.; Opila, R. L.; Bawendi, M. G.; Steigerwald, M. L.; Carroll, P. J.; Brus, L. E. *J. Am. Chem. Soc.* **1990**, 112, 1327.
- (15) Mews, A.; Eychmuller, A.; Giersig, M.; Schooss, D.; Weller, H. *J. Phys. Chem.* **1994**, 98, 934.
- (16) Danek, M.; Jensen, K. F.; Murray, C. B.; Bawendi, M. G. *Chem. Mater.* **1996**, 8, 173.
- (17) Littau, K. A.; Szajowski, P. J.; Muller, A. J.; Kortan, A. R.; Brus, L. E. *J. Phys. Chem.* **1993**, 97, 1224.
- (18) Wilson, W. L.; Szajowski, P. J.; Brus, L. E. *Science* **1993**, 262, 1242.
- (19) Hines, M. A.; Guyot-Sionnest, P. *J. Phys. Chem.* **1996**, 100, 468.
- (20) (a) Dabbousi, B. O.; Radzilowski, L. H.; Fogg D. E.; Mattoussi, H.; Rubner, M. F.; Schrock, R. R.; Thomas, E. L.; Bawendi, M. G. Manuscript in preparation. (b) Mattoussi, H.; Dabbousi, B. O.; Bawendi, M. G.; Rubner, M. F. Manuscript in preparation.
- (21) Rodriguez-Viejo, J.; Jensen, K. F.; Michel, J.; Mattoussi, H.; Dabbousi, B. O.; Bawendi, M. G. *Appl. Phys. Lett.* **1997**, 70, 2132.
- (22) The temperatures at which each individual size of dots was overcoated are as follows: 23 Å diameter (140 °C), 30 Å diameter (140 °C), 35 Å diameter (160 °C), 40 Å diameter (180 °C), 48 Å diameter (200 °C), 55 Å diameter (220 °C).
- (23) Fogg, D. E.; Radzilowski, L. H.; Blanski, R.; Schrock, R. R.; Thomas, E. L. *Macromolecules* **1997**, 30, 417.
- (24) Moulder, J. F.; Sticle, W. F.; Sobol, P. E.; Bomben, K. D. *Handbook of X-ray Photoelectron Spectroscopy*, Perkin-Elmer: 1993.
- (25) Kuno, M.; Lee, J. K.; Dabbousi, B. O.; Mikulec, F. V.; Bawendi, M. G. *J. Chem. Phys.* **1997**, 105, 9869.
- (26) In CdSe escape depths are 15 Å for the Cd 3d cores, 10 Å for Cd Auger, and 21 Å for the Se 3d cores. In ZnS the escape depths are 23.7 Å for Cd 3d cores, 13.2 Å for the Cd Auger, 31.2 Å for Se 3d cores, 9.6 Å for Zn 2p, 26.8 Å for Zn Auger, and 28.9 Å for S 2p core.
- (27) Bowen-Katari, J. E.; Colvin, V. L.; Alivisatos, A. P. *J. Phys. Chem.* **1994**, 98, 4109.
- (28) Hoener, C. F.; Allan, K. A.; Bard, A. J.; Campion, A.; Fox, M. A.; Mallouk, T. E.; Webber, S. E.; White, J. M. *J. Phys. Chem.* **1992**, 96, 3812.
- (29) Guinier, A.; Fournet, A. *Small Angle Scattering of X-rays*, J. Wiley & Sons: New York, 1955.
- (30) Kratky, O.; Glatter, O., Ed.; *Small Angle X-ray Scattering*; Academic Press: London, 1982.
- (31) Klug, H. P.; Alexander, L. E. *X-ray Diffraction Procedures*; Wiley: New York, 1954.
- (32) Murray, C. B. PhD thesis, Massachusetts Institute of Technology, 1996.
- (33) Kagan, C. R.; Murray, C. B.; Nirmal, M.; Bawendi, M. G. *Phys. Rev. Lett.* **1996**, 76, 1517.
- (34) Mattoussi, H.; Cumming, A. W.; Murray, C. B.; Bawendi, M. G.; Ober, R. *J. Chem. Phys.* **1996**, 105, 9890.
- (35) Haus, J. W.; Zhou, H. S.; Homma, I.; Komiyama, H. *Phys. Rev. B* **1993**, 47, 1359.
- (36) Schooss, D.; Mews, A.; Eychmuller, A.; Weller, H. *Phys. Rev. B* **1994**, 49, 49.
- (37) Nethercot, A. H. *Phys. Rev. Lett.* **1974**, 33, 1088.
- (38) We obtain an effective size distribution for the ZnS overcoated dots based on their absorption line widths by relating this line width to a size distribution of bare CdSe dots. To account for the size preference of the absorption into the larger particles, we convolute the PL peak with the cube of the effective radius (a^3) since the density of states is proportional to the volume of the dots. This results in a larger red-shift of the PL with increasing effective size distribution as observed experimentally.
- (39) Aven, M.; Prener, J. S. *Physics and Chemistry of II-VI Compounds*; North Holland: Amsterdam, 1967; p 144.
- (40) Zajicek, H.; Juza, P.; Abramof, E.; Pankratov, O.; Sitter, H.; Helm, H.; Brunthaler, G.; Faschinger, W.; Lischka, K. *Appl. Phys. Lett.* **1993**, 62, 717.